JOURNAL OF PROPULSION AND POWER
Vol. 18, No. 6, November–December 2002

Airfoil Row/Wake Interactions in a High-Speed Axial Compressor

Robert T. Johnston* and Sanford Fleeter†
Purdue University, West Lafayette, Indiana 47907

Experiments are performed to study and quantify the time-varying characteristics of inlet guide vane (IGV) wakes interacting with the exit flowfield of a downstream high-speed rotor. Data define the IGV wake pressure and velocity fields across two vane passages and time resolved over one rotor blade passing period. Results show that the interaction of the rotor wake with the IGV wake has a significant effect on both the IGV and rotor wakes. When the rotor wakes are in phase with the IGV wakes, the IGV wake velocity deficit, semiwake width, and total pressure losses increase. The maximum and minimum velocity and total pressure envelopes over one rotor blade passing period decrease with distance from the rotor due to the decay of the rotor wake. More importantly, the differences between the velocity and total pressure maximum and minimum are smaller in the IGV wake regions; therefore, the rotor wakes have reduced fluctuations. The position of the IGV wake centerline moves under the influence of the rotor cutting action and exit flowfield. The IGV vortical and potential harmonic gust forcing functions downstream of the rotor are determined by a vortical/potential gust splitting analysis. The first harmonic vortical and potential gust magnitudes have two maximums over one rotor blade passing period that occur before and after the IGV and rotor wakes are in phase. Also, the higher harmonics of the temporally averaged instantaneous vortical and potential gusts decay at a very slow rate as they propagate.

Nomenclature

A_n	=	potential disturbance nth harmonic constant
C	=	chord
D_n	=	vortical disturbance nth harmonic constant
$\boldsymbol{k}$	=	gust wave number vector
M	=	Mach number
p	=	static pressure perturbation
S	=	spacing
$\boldsymbol{U}$	=	absolute velocity vector
$\bar{\boldsymbol{U}}$	=	mean absolute velocity vector
u	=	axial velocity perturbation
v	=	tangential velocity perturbation
$\bar{\boldsymbol{W}}$	=	mean inlet guide vane (IGV)-relative velocity vector
W_{dc}	=	wake streamwise centerline velocity defect
W_0	=	freestream streamwise velocity
$\boldsymbol{w}$	=	perturbation velocity vector
$\boldsymbol{w}_{pn}, \boldsymbol{w}_{vn}$	=	nth harmonic potential and vortical gusts
$\boldsymbol{x}$	=	axial and tangential spatial coordinates, $\xi\hat{e}_\xi + \eta\hat{e}_\eta$
z	=	axial distance from IGV trailing edge
$\bar{\alpha}$	=	absolute flow angle
δ	=	semiwake width
ξ_u, ξ_d	=	axial distance upstream and downstream of the rotor
ϕ	=	potential function

Subscripts

I	=	IGV
m	=	measured
p	=	potential
R	=	rotor
v	=	vortical

Superscripts

$\bar{\ }$	=	mean
$\hat{\ }$	=	unit

Received 21 January 2002; revision received 24 July 2002; accepted for publication 30 July 2002.

*Postdoctoral Researcher, School of Mechanical Engineering, Purdue University; currently Instrumentation Technology Manager, Measurement Center/Engine Center, Pratt and Whitney, East Hartford, CT. Member AIAA.

†McAllister Distinguished Professor, School of Mechanical Engineering. Fellow AIAA.

Introduction

TURBOMACHINE design is based on models that assume steady relative flow through isolated airfoil rows. However, this is certainly not the case for multistage machines, wherein wakes have significant effects on downstream airfoil rows. For example, stationary airfoil wakes are cut by and convected through downstream rotating blade rows, which, in turn, have their wakes impinge on downstream stators or structural struts. Such wake/airfoil row interactions contribute to aerodynamic losses, pure tone noise, and rotor blade vibrations.

Blade/row interactions have been shown to have a significant impact on the flow in an axial flow compressor. For example, rotor wake passage through a downstream stator row results in total temperature variations. This is a result of rotor wake rectification due to their transport relative to the inviscid flow while passing through the stator row, with the stators collecting the rotor wakes on their pressure surfaces.[1] This mechanism is similar for stationary airfoil row wakes passing through a rotating blade row. Using computational fluid dynamics (CFD) and laser anemometer measurements, Shang et al.[2] showed that the circulation about rotor blades is dependent on rotor circumferential location due to the upstream potential field of a stator row. This phenomenon was found to be a strong function of rotor/stator spacing and relative blade counts.

Wake interactions in multistage turbomachines have been shown to have potential benefits with regard to performance and flow-induced vibrations. Turbine performance improvements were achieved by circumferentially indexing successive stator rows.[3] Peak efficiency occurred when the first vane row wake impinged on the second vane row after passing through the rotor, and minimum efficiency occurred when the first vane row wake passes between second stage vanes. Preliminary calculations indicated that the first vane wake was bowed exiting the rotor, thereby explaining the spanwise peak efficiency variation at different clocking positions.

Of particular interest herein is the potential beneficial effect of multistage wake interactions on blade row forced response. Specifically, airfoil/wake interactions are the most common and least understood source of unsteady aerodynamic excitation causing blade

row vibrations in multistage machines. In this regard, a model has been developed and utilized to demonstrate the feasibility of vane row indexing as a passive vibration control technique.[4] Correctly indexing stationary vane rows significantly reduced the unsteady aerodynamic forces, even for closely spaced airfoil rows.

To predict flow-induced vibrations of blade rows in a multistage environment accurately, thereby also making passive rotor vibration control techniques such as vane row indexing practical, a quantitative understanding of the time-varying characteristics of wakes interacting with downstream blade rows is required. Hence, this paper is directed at investigating the time-varying characteristics of inlet guide vane (IGV) wakes interacting with a downstream rotor for application to turbomachine forced response design systems. This is accomplished through a series of experiments performed in a high-speed fan stage comprising an IGV row and a rotor. This facility is ideal for these wake forcing function experiments because it is large enough for the necessary high-quality measurements, the IGV/rotor axial spacing is variable, and the IGV row can be indexed circumferentially, thereby enabling IGV wakes to be measured with stationary probes. With an IGV inlet Mach number of 0.29, the IGV wake unsteady pressure and velocity fields are measured with hot-film anemometers and dynamic total pressure probes. Data acquisition and analysis define the IGV wake pressure and velocity fields across two vane passages and as time resolved over one rotor blade passing period.

Axial Fan Facility

The Purdue Research Axial Fan facility features a 30.48-cm-(12-in.-) diam, $\frac{2}{3}$ hub/tip ratio design compressor rotor that is integral with the shaft. The drive system consists of a 400 hp ac motor driving a magnetic clutch, with a variable speed output that drives a gearbox (Fig. 1). There are 18 IGVs introducing swirl into a 19-blade axial flow rotor. Both the IGVs and rotor blades have NACA 65 series profiles on circular arc meanlines. Located approximately 3.5 rotor chords downstream of the rotor are eight aerodynamic structural struts (22% thick) that support the rotor bearing housing. Adjustable IGVs have a nominal 10% thickness with a chord varying from 35.5 mm (1.40 in.) at the hub to 53.3 mm (2.10 in.) at the tip, to yield a solidity of one. IGV twist distribution produces a free vortex whirl into the rotor. Rotor blade sections have a 10–6% hub-to-tip thickness taper, with a chord of 50.8 mm (2.00 in.). For these experiments, axial IGV-to-rotor spacing-to-chord ratios of $Z/C_R = 0.68$, 0.93, and 1.18 are investigated. The IGV row is indexed circumferentially, thereby enabling the IGV wake measurements to be made without circumferential probe traverses upstream and downstream of the rotor. Axial distance downstream of the IGV trailing edge at midspan is denoted as ξ, with the axial distance upstream of the rotor leading edge and downstream of the rotor trailing edge denoted by ξ_u and ξ_d. The compressor is operated at 10,000 rpm for these experiments, giving a total pressure ratio of 1.08 and at a flow rate of 3.8 kg/s (8.4 lb/s) ±2%.

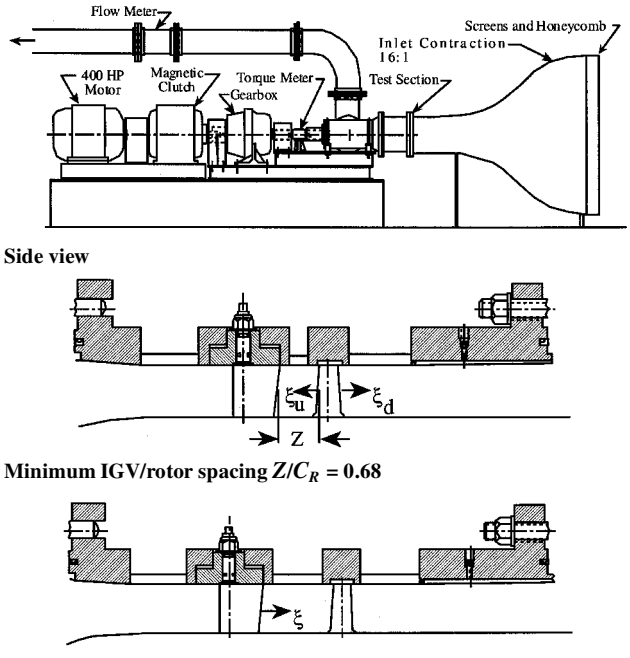

Fig. 1 Purdue high-speed axial compressor research facility.

Data Acquisition and Instrumentation

Downstream of the IGV row, the velocity and total pressure fields are measured to determine the IGV steady and unsteady characteristics. The midspan data are acquired in 1.0-deg increments in the freestream and 0.1-deg increments in the wakes. The wake regions are identified by first taking a traverse of two IGV passages with the coarse circumferential increments. Wake regions, once identified, are then resolved by taking measurements at smaller increments across each of two IGV wakes. Time-mean signals at each IGV azimuthal location are determined by taking the average of measurements of 80 rotor revolutions sampled at 1900 points per revolution for each data channel. At each of these azimuthal locations, the time-varying velocity and total pressure are also measured. The time-variant signals are digitized over 10 rotor blade passages using approximately 2000 samples per burst and are ensemble averaged over 200 individual revolutions, triggered by a once-per-revolution pulse from a photooptic sensor. These time-resolved velocity and total pressure data are then used to calculate the static pressure, assuming the flow is isentropic.

Midspan velocity and total pressure are measured downstream of the IGV with hot-film anemometers and total pressure probes designed to access the confined regions downstream of the rotor. An Endevco piezoresistive pressure transducer with a sensitivity of

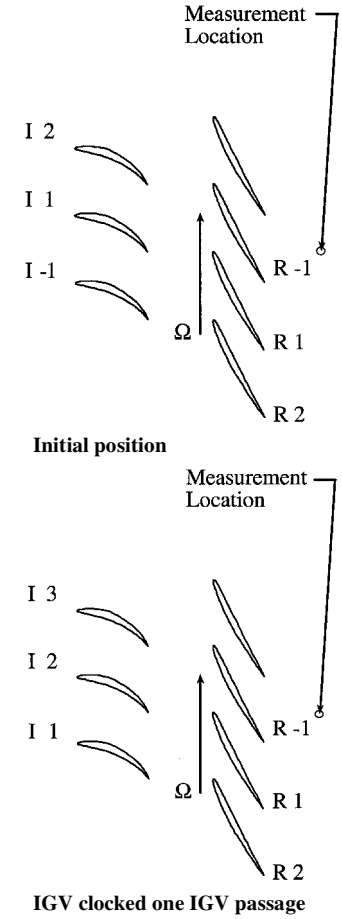

Fig. 2 Vane clocking and data processing schematic at start of data acquisition.

59.85 mV/psi and a frequency response of 70 KHz is installed in a stainless steel probe body. This design is capable of ±17-deg misalignment to the flow with less than ±−1% error in total pressure. The crossed hot film has a measurement area of 50.8 μm × 1.0 mm, with absolute velocity magnitude and flow angle errors estimated to be less than ±2% and ±0.5 deg, respectively. All probes are set to minimize flow angle deviations from the probe axis.

The IGV ring is traversed relative to the measurement location, as shown in Fig. 2. With the unsteady measurements initiated at the same rotor blade position for all IGV positions, the data are shifted in time to account for position of the rotor blades relative to $I2$. For measurements behind the trailing edge of vane $I1$, data acquisition is initiated when the leading edge of rotor blade $R1$ passes the measuring point. When $I2$ is upstream of the measurement location, the unsteady data acquisition is again initiated when $R1$ passes the probe. Thus, all locations, with the exception of the last azimuthal location, are time shifted by an amount proportional to the radial location and angular position relative to the final point and inversely proportional to the wheel speed. All Fig. 2 plots shown of the IGV wake are viewed from the measurement location looking upstream.

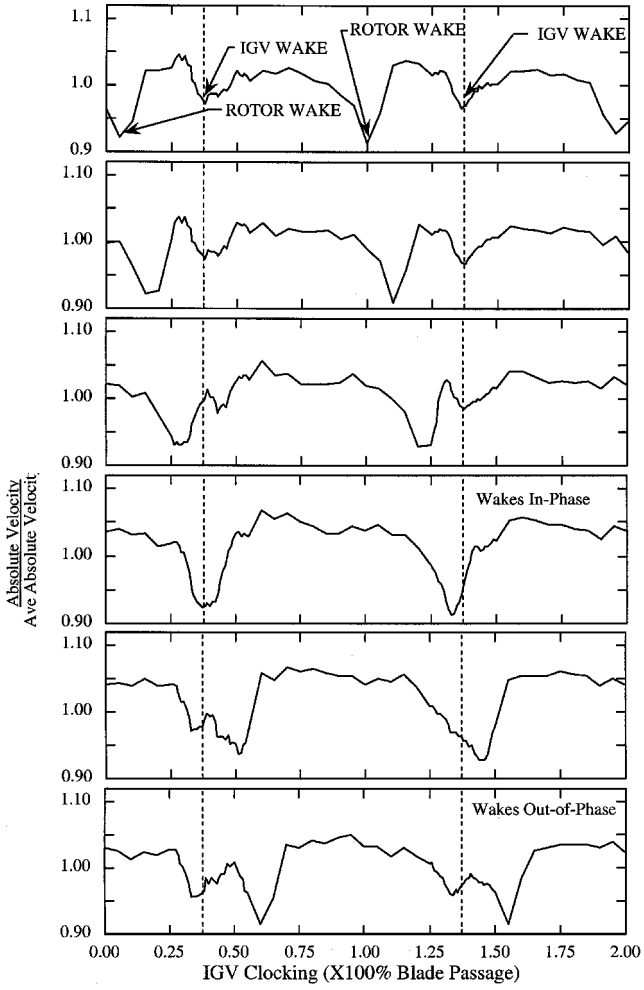

Fig. 3 Rotor wake/IGV wake interaction at equal time increments, $\xi_d/S_R = 0.22$ and $Z/C_R = 0.93$.

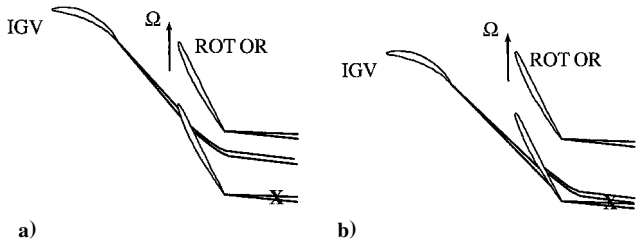

Fig. 4 Sketch showing IGV wake a) out of phase and b) in phase for a probe at position X.

Vortical/Potential Gust Splitting Analysis

The two-dimensional inviscid flow is assumed to be compressible, isentropic, and composed of an absolute mean velocity $\bar{U}$ with superimposed small velocity $\boldsymbol{w}$ and static pressure spatial perturbations p. The linearized continuity and momentum equations are

$$\frac{1}{c_0^2}\frac{\bar{\mathrm{D}}p}{\mathrm{D}t} + \bar{\rho}\nabla\times\boldsymbol{w} = 0, \qquad \bar{\rho}\frac{\bar{\mathrm{D}}\boldsymbol{w}}{\mathrm{D}t} + \nabla p = 0 \tag{1}$$

Vortical/Potential Splitting

The perturbation velocity field is split into vortical and potential gust components $\boldsymbol{w} = \boldsymbol{w}_p = \boldsymbol{w}_v$, which satisfy

$$\frac{\bar{\mathrm{D}}\boldsymbol{w}_v}{\mathrm{D}t} = 0, \qquad \nabla\times\boldsymbol{w}_v = 0 \tag{2}$$

$$\rho\frac{\bar{\mathrm{D}}\boldsymbol{w}_p}{\mathrm{D}t} = -\nabla_p, \qquad \frac{1}{\rho c_0^2}\frac{\bar{\mathrm{D}}p}{\mathrm{D}t} = -\nabla\times\boldsymbol{w}_p, \qquad \nabla\times\boldsymbol{w}_p = 0 \tag{3}$$

Thus, the forcing function is analyzed harmonically as a Fourier series of individual vortical and potential gusts,

$$\boldsymbol{w}(\boldsymbol{x}, t) = \sum[\boldsymbol{w}_{vn}(\boldsymbol{x}) + \boldsymbol{w}_{pn}(\boldsymbol{x})]e^{in\omega x}$$

Vortical Gust

Spatial periodicity shows that the gust wave number vector $\boldsymbol{k}$ must be perpendicular to the IGV mean flow exit velocity vector $\bar{\boldsymbol{U}}$:

$$\boldsymbol{k}\times\bar{\boldsymbol{U}} = 0 \tag{4}$$

where $\bar{\boldsymbol{U}} = \bar{U}(\cos\bar{\alpha}\hat{e}_\xi + \sin\bar{\alpha}\hat{e}_\eta)$.

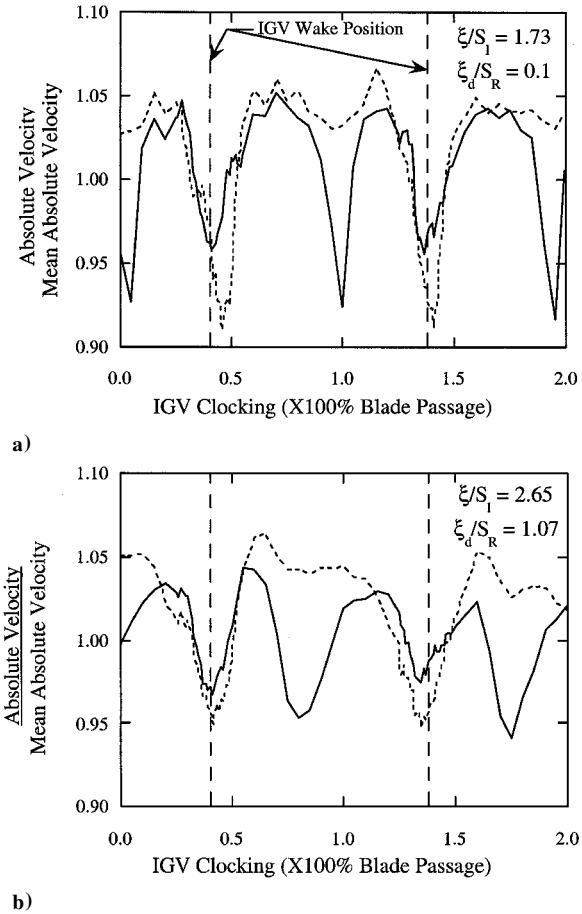

Fig. 5 Rotor wake/IGV wake in phase ——, and out of phase - - - -, at two axial locations downstream of the rotor ($Z/C_R = 0.93$).

Periodicity requirements determine the tangential wave number $k_\eta = 2\pi/S_I$, with the axial wave number then determined from Eq. (4), $k_\xi = -k_\eta \tan\bar{\alpha}$. The vortical gust convects with the mean flow $\bar{U}$. This and $\nabla \times \boldsymbol{w}_v = 0$ relate the wave number vector and the gust amplitude vector such that the gust is oriented in a direction normal to $\boldsymbol{w}_{vn}$. Combining this with Eq. (4) shows that the vortical gust amplitude vector must be parallel to the mean velocity. Denoting the complex constant of proportionality between these two constant vectors by D_n^* leads to

$$\boldsymbol{w}_{vn} = D_n^* \bar{U}(\cos\bar{\alpha}\hat{e}_\xi + \sin\bar{\alpha}\hat{e}_\eta)\exp(-in\boldsymbol{k}\times\boldsymbol{x}) \tag{5}$$

Thus, the vortical gust propagates unattenuated in the direction of the gust wave number vector $\boldsymbol{k}$. This defines the vortical gust velocity perturbation with all parameters known from measurements, except for D_n^*, which must be calculated for each harmonic.

Potential Gust

The potential gust $\boldsymbol{w}_p$ must satisfy $\nabla \times \boldsymbol{w}_p = 0$; therefore, it can be derived from a potential function, $\boldsymbol{w}_p = \nabla\phi_p$. The perturbation potential is related to the pressure perturbation p through the unsteady Bernoulli equation. Substituting these relations into Eq. (1) yields the following perturbation velocity potential equation:

$$\frac{1}{c_0^2}\frac{\bar{\mathrm{D}}}{\mathrm{D}t}\left(\frac{\bar{\mathrm{D}}\phi_p}{\mathrm{D}t}\right) - \nabla^2\phi_p = 0 \tag{6}$$

Because the flow is steady, the potential gust solution, determined from the steady form of this equation, is

$$\phi_{pn} = A_n \exp[n(\chi k_\eta \xi - ik_\eta \eta)] \tag{7}$$

where

$$\chi = \frac{-iM^2\sin\bar{\alpha}\cos\bar{\alpha} \pm \sqrt{1-M^2}}{1-M^2\cos^2\bar{\alpha}}$$

is the axial decay factor and A_n is a complex constant.

Thus, the potential gust is spatially periodic in the tangential direction, but decays exponentially in the axial direction. The direction of this axial decay depends on whether an upstream or downstream blade row is being analyzed. The potential static pressure perturbation is found from the unsteady Bernoulli equation:

$$p_{pn}/\rho\bar{U}^2 = A_n^*(-\chi\cos\bar{\alpha} + i\sin\bar{\alpha})\exp[n(\chi k_\eta\xi - ik_\eta\eta)] \tag{8}$$

Experimental Determination of D_n^* and A_n^*

The potential gust $\boldsymbol{w}_{pn}$ is irrotational. Therefore, the vorticity γ_{pn} is zero, $|\gamma_{pn}| = |\nabla \times \boldsymbol{w}_{pn}| = 0$, and p_{pn} is given in Eq. (8). Thus, the potential gust manifests itself in both static pressure and velocity spatial perturbations, but not in the vorticity perturbation. The vorticity of the vortical gust is

$$|\gamma_{vn}| = |\nabla \times \boldsymbol{w}_{vn}| = D_n^*(ink_\eta\bar{U}/\cos\bar{\alpha})\exp(-in\boldsymbol{k}\times\boldsymbol{x})$$

and there is no corresponding static pressure perturbation. This vortical gust component, therefore, manifests itself in a vorticity perturbation, but not in the static pressure perturbation.

The spatial static pressure perturbation is dependent only on the potential gust. At the measurement location $(\xi, \eta) = (0, 0)$, the potential gust coefficient A_n^*, computed explicitly from the calculated static pressure, is

$$A_n^* = p_{mn}/[\rho\bar{U}^2(-\chi\cos\bar{\alpha} + i\sin\bar{\alpha})] \tag{9}$$

where p_{mn} is the measured nth harmonic static pressure spatial perturbation.

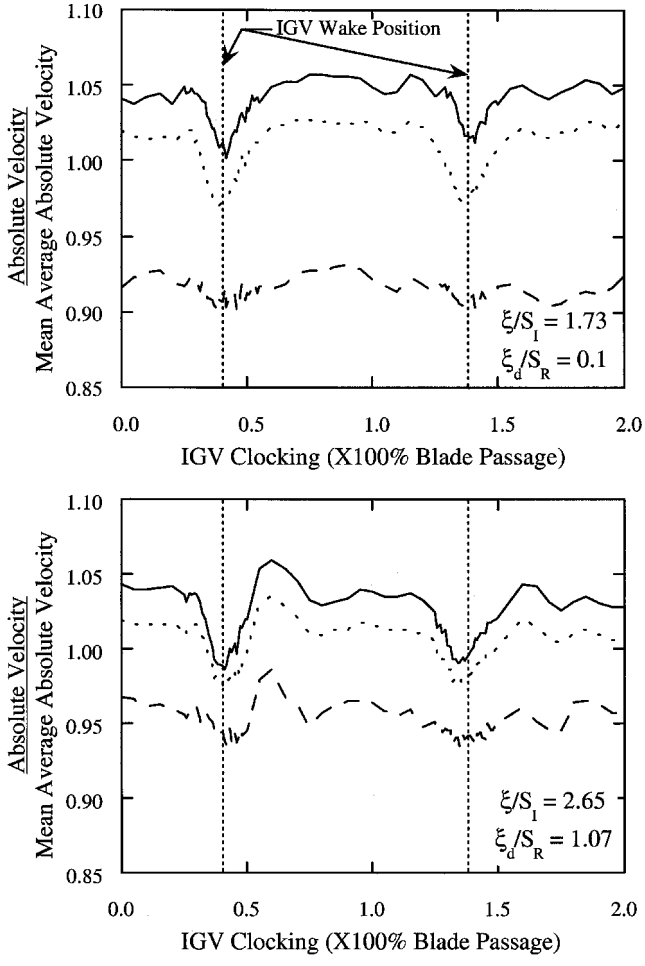

Fig. 6 Maximum ——, minimum – – –, and average - - - -, velocity over two vane passages for one rotor blade passing period (Z/C_R = 0.93).

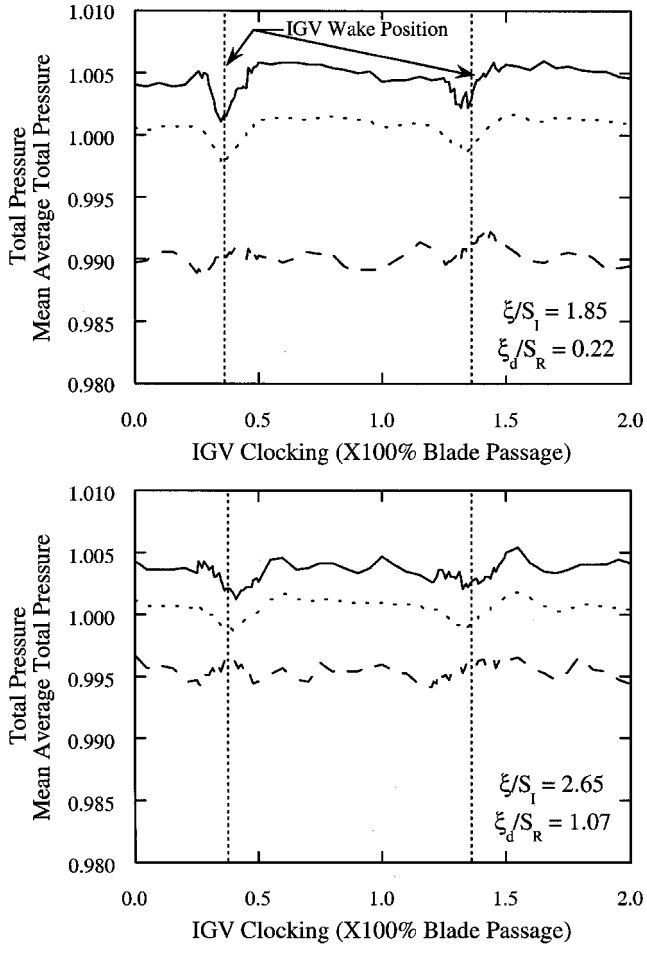

Fig. 7 Maximum ——, minimum – – –, and average - - - -, total pressure over two vane passages for one rotor blade passing period (Z/C_R = 0.93).

The potential gust velocity perturbation is then calculated and subtracted from the measured velocity perturbation to yield a difference velocity perturbation.[5] Because the vorticity of the potential component is zero, the perturbation of the velocity difference has the same vorticity as the measured gust. Thus, the linear theory vortical gust coefficient is calculated from this difference velocity perturbation as

$$D_n^* = (1/U)(u_{dn}\cos\bar{\alpha} + v_{dn}\sin\bar{\alpha}) \tag{10}$$

Results

To provide a quantitative understanding of wake/blade row interactions for application to forced response design, a series of experiments is performed directed at investigating the time-varying characteristics of IGV wakes interacting with the exit flow from a downstream high-speed rotor. With an IGV inlet Mach number of 0.29 and a 0.6 rotor inlet relative Mach number at midspan, the IGV wake unsteady pressure and velocity fields are measured with hot-film anemometers and dynamic total pressure probes. Flow coefficient is calculated from these measurements to be 0.74. Data acquisition and analysis define the IGV wake pressure and velocity fields across two vane passages and is time resolved over one rotor blade passing period. The instantaneous IGV wake characteristics are examined, with the interaction effects characterized by analysis of velocity deficit and semiwake width data at critical rotor blade positions. The position of the IGV wake centerline is measured to determine the dependence on the rotor cutting action and the rotor exit flowfield. Linear theory analysis is then used to split the time-varying IGV wake into vortical and potential components, and these gust component data are then analyzed. Estimated uncertainty in the calculation for A_n^* and D_n^* are ±2.6 and ±2.9%, respectively.

Time-Resolved IGV Wake Characteristics

Figure 3 shows a time sequence of the instantaneous absolute velocity downstream of the rotor over two vane passages, with the data presented from the IGV pressure to suction surface. This represents the flowfield at the measurement point at several rotor positions as the IGV is traversed. The rotor blade cuts the IGV wake at specific rotor positions. As time progresses, the IGV wake passes between the rotor blades and convects downstream. The wakes are said to be

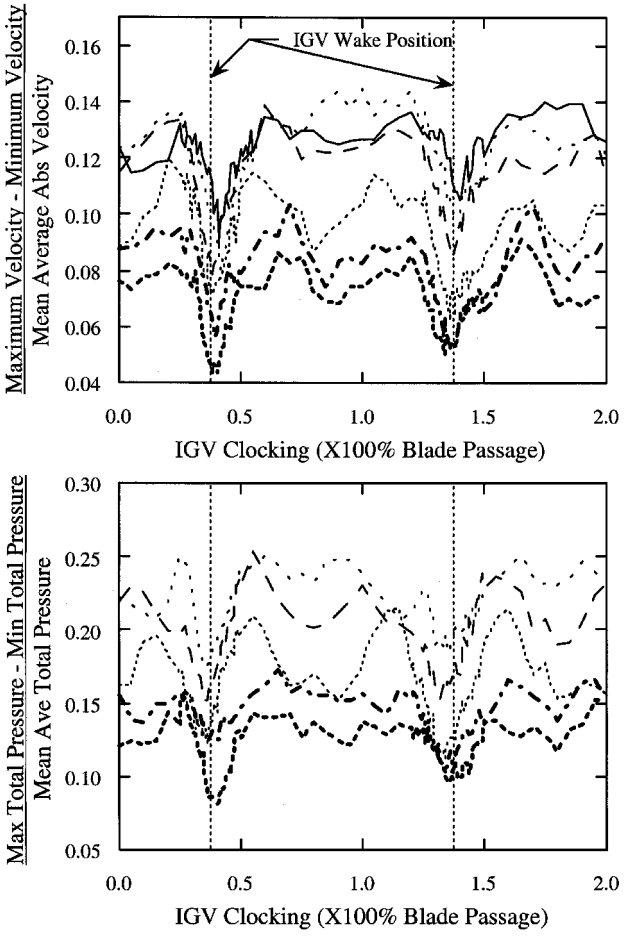

Fig. 8 Difference between maximum and minimum velocity and total pressure across two vane passages over one rotor blade passing period (Z/C_R = 0.93): ——, ξ/S_I = 1.73 and ξ_d/S_R = 0.1; · · · ·, ξ/S_I = 1.85 and ξ_d/S_R = 0.22; — — -, ξ/S_I = 1.96 and ξ_d/S_R = 0.34; ····, ξ/S_I = 2.19 and ξ_d/S_R = 0.58; - - -, ξ/S_I = 2.42 and ξ_d/S_R = 0.82; and •••, ξ/S_I = 2.65 and ξ_d/S_R = 1.07.

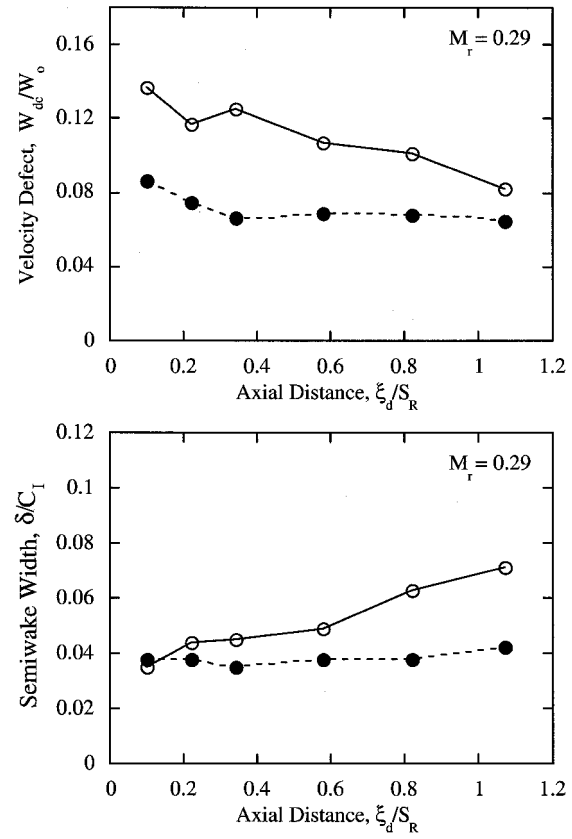

Fig. 9 IGV wake velocity deficit and semiwake width when in phase ○, and out of phase ●, with the rotor wake (Z/C_R = 0.93).

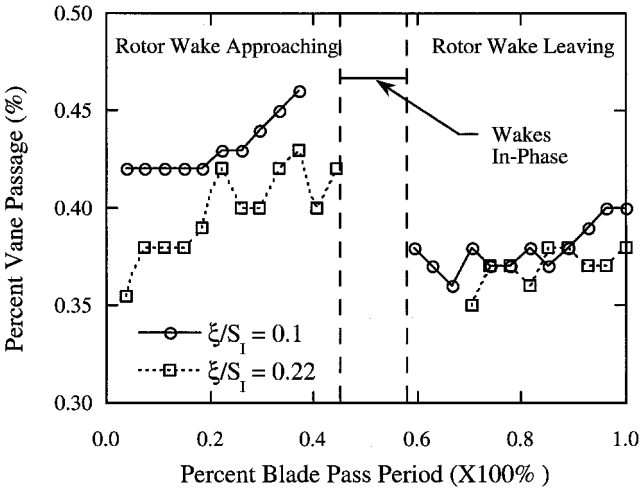

Fig. 10 IGV wake centerline position at two axial locations downstream of the rotor during one rotor blade passing period (Z/C_R = 0.93).

out of phase when they appear as distinct features downstream of the rotor (Fig. 4a). When the rotor and IGV wakes are in phase (meaning the rotor blade wake actually combines with the IGV wake), a large, wide velocity deficit is evident at both IGV wake locations (Fig. 4b). Note that there is minimal variation in the rotor wake minimum velocities as they pass through the IGV wakes. Because the ratio of the number of IGVs to the number of rotor blades is not unity, $N_{\text{vanes}}/N_{\text{blades}} = 0.947$, the rotor/IGV wake interaction does not occur simultaneously for both IGV wakes shown in Figs. 4. Also, because the measurement spatial resolution is higher in the IGV wake regions, the narrow rotor wakes are somewhat crudely defined in the IGV exit flow freestream regions.

The IGV wake absolute velocity downstream of the rotor at axial positions closest to and farthest from the rotor detail the in-phase and out-of-phase rotor exit flowfield wake characteristics (Fig. 5). The position of the IGV wake centerline in Fig. 5a is marked by a dashed line. The IGV wake velocity deficit and semiwake width are clearly smaller when the IGV and rotor wakes are out of phase. It is again evident that the minimum rotor wake velocity is relatively independent of whether it is in or out of the IGV wake.

Figures 6 and 7 present the level of the absolute velocity and total pressure fluctuations downstream of the rotor. Maximum, minimum, and average absolute velocity for two vane passages over one rotor blade passing period are shown at two axial locations. The envelopes of the maximum/minimum velocity and total pressure are largest for the data closest to the rotor trailing edge and smallest farther downstream. This is expected because the rotor wake velocity deficit is directly associated with the flow fluctuations, and it decays with distance from the trailing edge. Note that the maximum velocity curve is reduced in the IGV wake region, whereas the minimum velocity curve does not undergo similar reductions in the IGV wake region.

The differences between the maximum and minimum absolute velocity and total pressure measured at a number of locations downstream of the rotor reveals that these fluctuations are reduced in the region of the IGV wakes (Fig. 8). This indicates that the rotor wake velocity deficit is reduced by the IGV/rotor wake interaction. Also, the velocity difference decreases with distance from the rotor as a result of the decay of the rotor wakes.

The features of the time-resolved IGV wakes are characterized by the semiwake width δ and IGV wake centerline velocity deficit

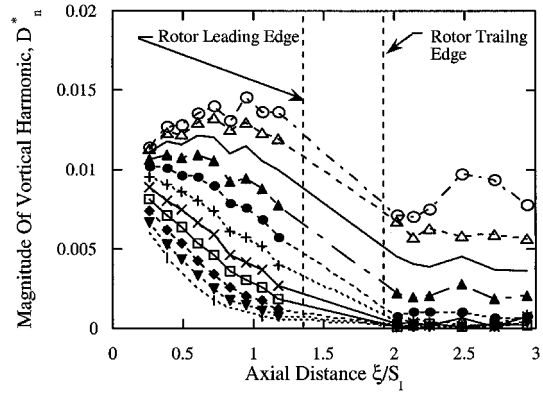

Fig. 12 Decay of the higher harmonics of the steady IGV wake vortical gust component in the axial direction ($Z/C_R = 1.18$): ○, D_1^*; △, D_2^*; ——, D_3^*; ▲, D_4^*; ●, D_5^*; +, D_6^*; ×, D_7^*; □, D_8^*; ◆, D_9^*; ▼, D_{10}^*; and ▌, D_{11}^*.

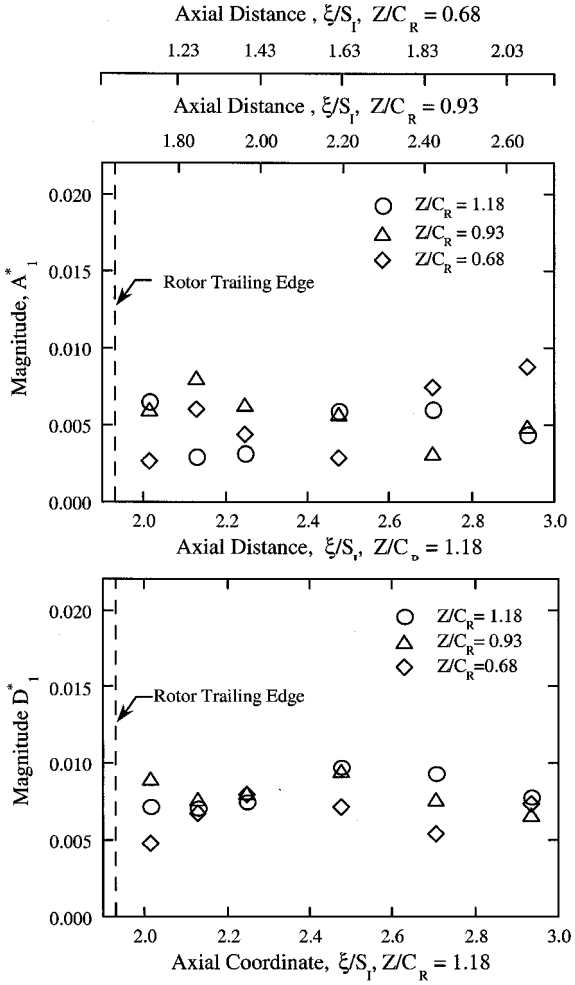

Fig. 11 Axial behavior of the steady flow first harmonic potential and vortical gust component downstream of the rotor.

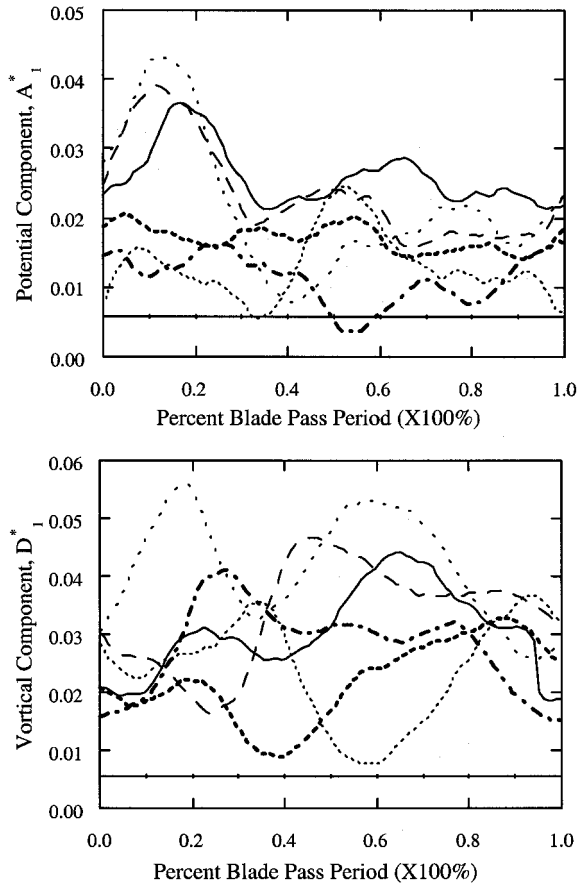

Fig. 13 Time variation of the IGV wake first harmonic magnitude ($Z/C_R = 0.93$): ——, $\xi/S_I = 1.73$ and $\xi_d/S_R = 0.1$; · · · ·, $\xi/S_I = 1.85$ and $\xi_d/S_R = 0.22$; — — -, $\xi/S_I = 1.96$ and $\xi_d/S_R = 0.34$; ····, $\xi/S_I = 2.19$ and $\xi_d/S_R = 0.58$; - · -, $\xi/S_I = 2.42$ and $\xi_d/S_R = 0.82$; -···-, $\xi/S_I = 2.65$ and $\xi_d/S_R = 1.07$; and —+—, steady flow.

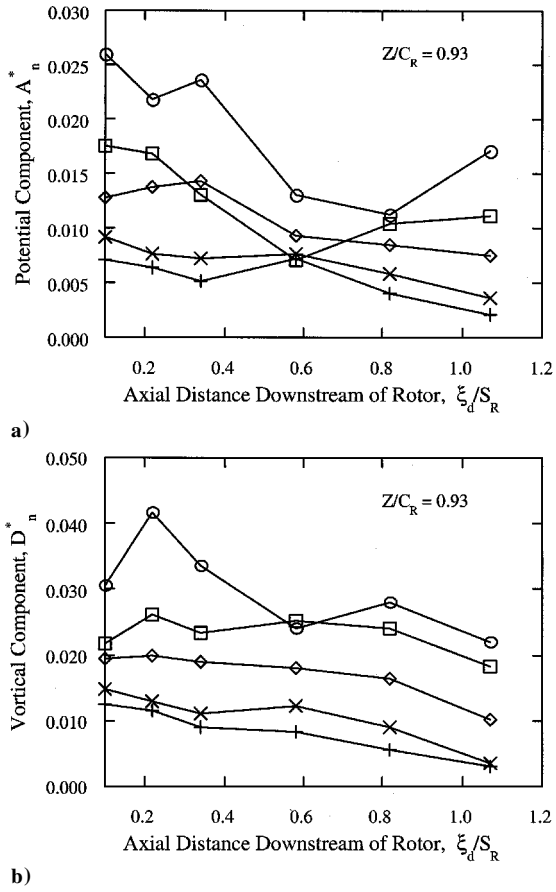

Fig. 14 Decay of the harmonics of the time-averaged instantaneous a) vortical (○, A_1^*; □, A_2^*; ◇, A_3^*; ×, A_4^*; and +, A_5^*) and b) potential (○, D_1^*; □, D_2^*; ◇, D_3^*; ×, D_4^*; and +, D_5^*) components of the IGV.

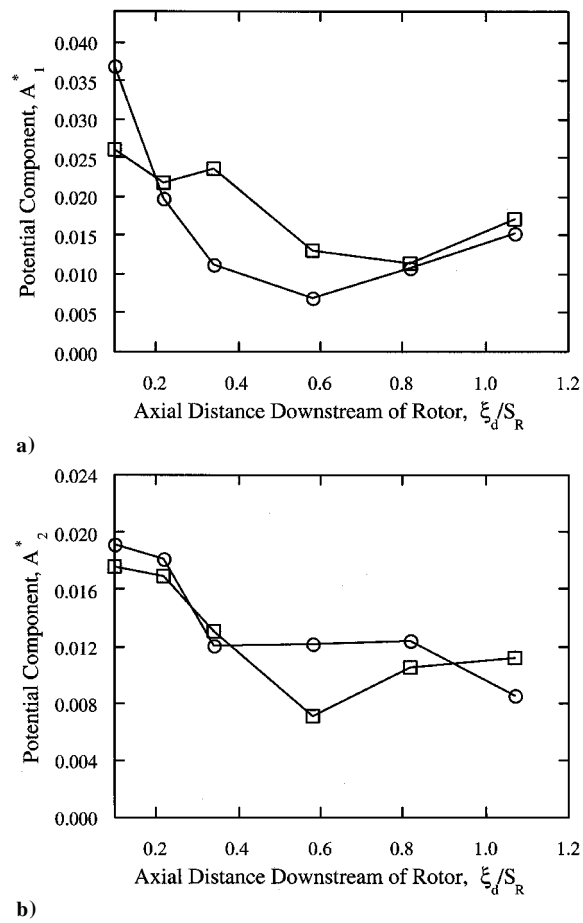

Fig. 15 Comparison of the time-averaged instantaneous potential components a) ○, A_1^*, Z/C_R = 0.68 and □, A_1^*, Z/C_R = 0.93 and b) ○, A_2^*, Z/C_R = 0.68 and □, A_2^*, Z/C_R = 0.93 for two axial spacings.

W_{dc} when the IGV and rotor wakes are in phase and out of phase (Fig. 9). The IGV wake velocity deficit is much larger when the IGV and rotor wakes are in phase. Also, it decreases with distance downstream of the rotor, but at a much higher rate when the IGV and rotor wakes are in phase. This is because the rotor wake velocity deficits are decreasing at a greater rate than the older, more slowly decaying IGV wakes. The IGV semiwake width increases with distance downstream of the rotor when the IGV and rotor wakes are in phase, a result of the increase of the rotor semiwake width. However, the IGV semiwake width remains relatively constant when the IGV and rotor wakes are out of phase.

Careful inspection of Fig. 3 reveals that the IGV wake centerline (point of minimum velocity) is not constant during one rotor blade passing period. The IGV wake centerline position is measured at a number of times over one rotor blade passing period when the IGV/rotor wakes are not in phase, as is shown in Fig. 10. Measurements are presented for the two locations closest to the rotor trailing edge, $\xi_d/S_R = 0.1$ and 0.22. As the rotor wake approaches the IGV wake, the IGV wake centerline moves in the direction of travel of the advancing rotor blade. Once the wakes are no longer in phase, the IGV wake centerline has moved to a position that is the minimum over the rotor blade passing period. Physical mechanisms responsible for the motion of the IGV wake centerline are the cutting of the IGV wake by the rotor blades and the effect of the rotor blade exit flowfield on the IGV wake. Further study is needed to determine which mechanism is dominant.

Steady Flow IGV Wake Vortical/Potential Splitting

To clearly show the effects of the interaction of the IGV wakes with the downstream rotor flowfield, steady flow IGV wake nondimensional potential and vortical gust component data are considered. The effects of IGV/rotor axial spacing on the steady IGV wake first harmonic potential and vortical gusts are shown in Fig. 11. The magnitude of the IGV potential gust A_1^* decays exponentially upstream of the rotor.[6] However, it decays to a relatively constant, but nonzero, value, which is still evident downstream of the rotor. This is due to either the large total pressure gradients or propagating acoustic modes that arise from rotor/stator interactions.[6] The IGV wake vortical gust magnitude D_1^* is significantly reduced by the interaction with the rotor and is relatively constant downstream of the rotor as predicted by the theory. Also, the IGV/rotor axial spacing has only a minimal effect on the magnitudes of A_1^* and D_1^*.

The steady IGV wake vortical gust component has a significant higher harmonic content that must be considered (Fig. 12). Upstream of the rotor, the magnitudes of the first three harmonics remain relatively constant, whereas the magnitudes of the fourth and higher components decay at a nearly uniform rate. The small increase in the first harmonic magnitude as the rotor is approached is due to energy being transferred from the higher harmonics to the lower harmonics as the wakes decay. After the IGV wakes pass through the rotor, the first five IGV vortical gust harmonics are still apparent and remain constant with axial location. However, they are significantly reduced. Harmonics above the fifth are reduced to zero by the interaction with the rotor.

Time-Resolved IGV Wake Vortical/Potential Gusts

The time-resolved IGV wake first harmonic potential A_1^* and vortical D_1^* gust magnitudes over one rotor blade passing period downstream of the rotor are shown in Fig. 13. The interaction with the rotor has a significant effect on the magnitudes of A_1^* and D_1^*. Namely, at all axial locations, A_1^* and D_1^* are greater in magnitude than the corresponding steady flow values.

The magnitudes of A_1^* and D_1^* vary over one rotor blade passing period at each axial location, with A_1^* and D_1^* generally decreasing with downstream distance. Maximums in both the vortical and

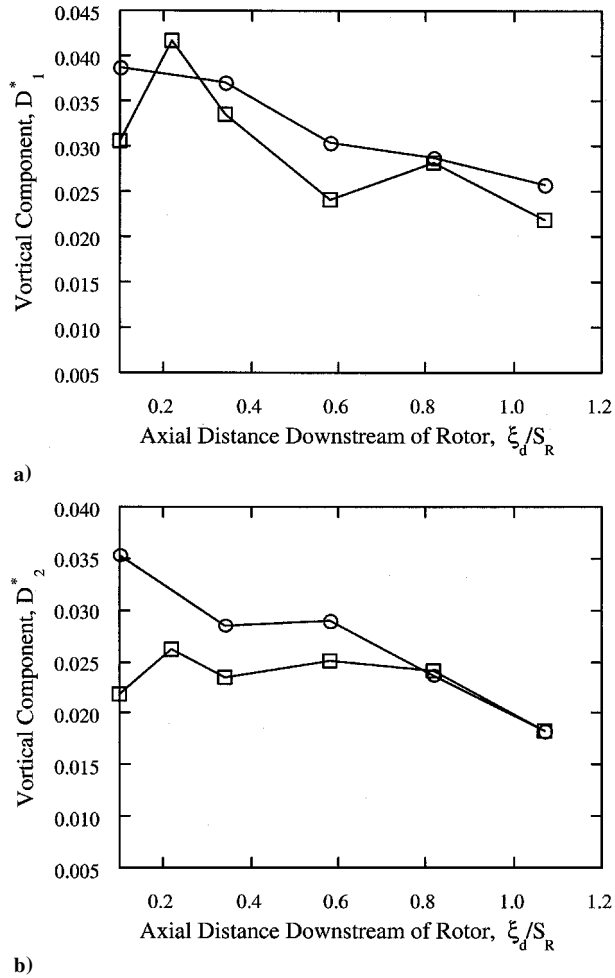

Fig. 16 Comparison of the time averaged instantaneous vortical components a) ○, D_1^*, Z/C_R = 0.68 and □, D_1^*, Z/C_R = 0.93 and b) ○, D_2^*, Z/C_R = 0.68 and □, D_2^*, Z/C_R = 0.93 for two axial spacings.

potential gusts occur twice over one rotor blade passing period, before and just after the IGV and rotor wakes are in phase. The locations of these minimums and maximums vary in time for each axial location due to the initial azimuthal location of the rotor wake changing with axial position, that is, as the axial position is varied, the IGV and rotor wakes are in phase at different times after the trigger signal due to the change in the position of the rotor wake relative to the IGV wake.

The relationship between the time-averaged instantaneous magnitudes of A_n^* and D_n^* and the proximity of the rotor is shown in Fig. 14. Presented is the time-averaged instantaneous magnitude of the first five harmonics of the IGV wake vortical and potential gust averaged over one rotor blade passing period. The time-averaged instantaneous values of both A_n^* and D_n^* generally decrease with increasing axial distance from the rotor, with the exception of A_1^*. Figures 15 and 16 show the magnitudes of the first two harmonics of the potential A_n^* and vortical D_n^* gust components for two rotor/IGV axial spacings. Evident is the good agreement in these first two harmonics for both the vortical and potential gusts. The increase in the first harmonic of the potential gust magnitude as the structural struts are approached is evident at both IGV/rotor spacings shown in Fig. 15. This increase may be the result of acoustic modes generated by the rotor wake/structural strut interaction.

Summary

This paper was directed at investigating the time-varying characteristics of IGV wakes interacting with the flowfield from a downstream rotor for application to turbomachine forced response design systems. This was accomplished through a series of experiments performed in a high-speed fan stage comprising an IGV row and a downstream rotor. With an IGV inlet Mach number of 0.29, the IGV wake unsteady pressure and velocity fields were measured with hot-film anemometers and dynamic total pressure probes. Data acquisition and analysis defined the IGV wake pressure and velocity fields across two vane passages and as time resolved over one rotor blade passing period.

The rotor wake was observed to move tangentially toward and then slowly engulf the IGV wake. As time progressed, the rotor wakes moved out of the IGV wake and into the out-of-phase position. There was minimal variation in the minimum velocity in the rotor wake as it traversed the IGV wakes. Data also defined the IGV wake semiwake width and centerline velocity deficit with the IGV and rotor wakes both in phase and out of phase. When the IGV and rotor wakes were in phase, the velocity deficit was much larger and decreased with distance downstream of the rotor at a much higher rate than the out-of-phase condition. The IGV wake width increased as the distance from the rotor increased when the wakes were in phase due to the growth of the rotor wake. When the IGV and rotor wakes were out of phase, the IGV wake width remained relatively constant. The position of the IGV wake centerline was observed to move due to the effect of the rotor cutting action and the rotor exit flowfield.

The fluctuations of the absolute velocity and total pressure downstream of the rotor were reduced in the region of the IGV wakes, indicating that the rotor wake velocity deficit was reduced by the IGV/rotor wake interaction. Also, the velocity difference decreased with distance from the rotor as a result of the decay of the rotor wakes.

Steady flow IGV wake potential gust A_1^* decays exponentially upstream of the rotor to a relatively constant, but nonzero, value, which is still evident downstream of the rotor. This is due to either the large total pressure gradients or propagating acoustic modes that arise from rotor/stator interactions. The IGV wake vortical gust magnitude D_1^* is significantly reduced by the interaction with the rotor and is relatively constant downstream of the rotor as predicted by the theory. Also, the IGV/rotor axial spacing has only a minimal effect on the magnitudes of A_1^* and D_1^* downstream of the rotor. That is, this upstream blade row spacing will not be a major consideration when placing stators downstream of the rotor.

Time-varying IGV wake first harmonic potential and vortical gust magnitudes over one rotor blade passing period generally decreased in magnitude with distance downstream of the rotor due to the decay of the rotor wakes. The magnitudes of A_1^* and D_1^* at all axial locations downstream of the rotor were greater than the corresponding steady flow values because of the unsteady interaction with the rotor wake. Values of A_1^* and D_1^* at each axial location varied over one rotor blade passing period, and maximums in both the vortical and potential gusts occurred twice over one rotor blade passing period, before and just after the IGV and rotor wakes being in phase. The instantaneous magnitudes of the first five harmonics of the vortical and potential gusts averaged over one rotor blade passing period generally decreased with increasing axial distance from the rotor. Also, comparisons of data for the two smallest rotor/IGV axial spacings were in agreement. Values of A_1^* time averaged over one rotor blade passing period increased in magnitude as the structural struts are approached.

The results from this experiment could be used to help predict the optimum vane indexing position for a stator row placed downstream of the rotor in future tests. The best indexing location would depend on the number of stators selected for that row; however, if the blade count were identical to the IGV count, then the velocity and pressure fluctuations experienced by the stator row would be minimized at midspan if indexing were done to place the stator vanes in the wakes of the upstream IGV.

This fundamental series of experiments indicates that airfoil wake/rotor interactions, which occur in multistage machines, can result in rotor exit flowfields that are potentially more harmful with regard to the fatigue life of downstream blade rows than is predicted by current design practice, which ignores wake interactions and assumes steady flow through isolated airfoil rows.

Acknowledgment

This research was sponsored by the GUIde Consortium on Bladed Disk Forced Response.

References

[1]Kerrebrock, J. L., and Mikolajczak, A. A., "Intra-Stator Transport of Rotor Wakes and Its Effect on Compressor Performance," *Journal of Engineering for Power*, Vol. 92, Oct. 1970, pp. 359–368.

[2]Shang, T., Epstein, A. H., Giles, M. B., and Sehra, A. K., "Blade/Row Interaction Effects on Compressor Measurements," *Journal of Propulsion and Power*, Vol. 9, No. 4, 1993, pp. 569–578.

[3]Huber, F. W., Johnson, D., Sharma, O. P., Stauback, J. B., and Gaddis, S. W., "Performance Improvement Through Indexing of Turbine Airfoils Part 1—Experimental Investigation," American Society of Mechanical Engineers, ASME Paper 95-GT-27, June 1995.

[4]Sanders, A., and Fleeter, S., "Vane Row Indexing for Passive Vibration Control of Axial Flow Turbomachine Rotors," *Journal of Propulsion and Power*, Vol. 15, No. 5, 1999, pp. 650–657.

[5]Feiereisen, J. M., and Fleeter, S., "Low Solidity Vane Unsteady Aerodynamic Response to Combined Vortical–Potential Forcing Functions," AIAA Paper 94-2974, June 1994.

[6]Johnston, R. T., and Fleeter, S., "Inlet Guide Vane Wakes, Including the Effect of the Rotor," *Journal of Fluids and Structures*, Vol. 15, No. 2, 2001, pp. 235–254.